



A GX₂GX₃G motif facilitates acyl chain sequestration by *Saccharomyces cerevisiae* acyl carrier protein

Received for publication, June 1, 2021, and in revised form, November 3, 2021. Published, Papers in Press, November 9, 2021.
<https://doi.org/10.1016/j.jbc.2021.101394>

Garima[‡], Rashima Prem[‡], Usha Yadav, and Monica Sundd^{*✉}

From the NMR Lab, National Institute of Immunology, New Delhi, India

Edited by Wolfgang Peti

Saccharomyces cerevisiae acyl carrier protein (ScACP) is a component of the large fungal fatty acid synthase I (FAS I) complex. ScACP comprises two subdomains: a conserved ACP domain that shares extensive structural homology with other ACPs and a unique structural domain. Unlike the metazoan type I ACP that does not sequester the acyl chain, ScACP can partially sequester the growing acyl chain within its hydrophobic core by a mechanism that remains elusive. Our studies on the acyl-ScACP intermediates disclose a unique ¹⁸⁸GX₂GX₃G¹⁹⁵ sequence in helix II important for ACP function. Complete loss of sequestration was observed upon mutation of the three glycines in this sequence to valine (G188V/G191V/G195V), while G191V and G188V/G191V double mutants displayed a faster rate of acyl chain hydrolysis. Likewise, mutation of Thr216 to Ala altered the size of the hydrophobic cavity, resulting in loss of C₁₂- chain sequestration. Combining NMR studies with insights from the crystal structure, we show that three glycines in helix II and a threonine in helix IV favor conformational change, which in turn generate space for acyl chain sequestration. Furthermore, we identified the primary hydrophobic cavity of ScACP, present between the carboxyl end of helix II and IV. The opening of the cavity lies between the second and third turns of helix II and loop II. Overall, the study highlights a novel role of the GX₂GX₃G motif in regulating acyl chain sequestration, vital for ScACP function.

Fatty acid biosynthesis is an important cellular process, indispensable for membrane biogenesis, cell metabolism, and generation of signaling molecules. Based on the organization, fatty acid biosynthetic machinery has been categorized into (a) dissociated type (type II pathway) observed in prokaryotes, plastids, and mitochondria; and (b) type I pathway, found in eukaryotes and a few bacterial species. Each catalytic unit is an independent protein in the type II pathway. On the contrary, type I pathway enzymes exist as domains of a large, multifunctional fatty acid synthase (FAS). Within the type I FAS, two different subtypes have been identified: a 540 kDa homodimer present in metazoans, while in yeast/fungi/actinomycetes, a 2.6 MDa dodecameric (α6β6) complex is present. The complex forms a barrel-shaped structure with

six β-subunits, three on either side of a central disc formed by six α-subunits (1, 2). Seven catalytically active centers and the ACP domain may be present on a single polypeptide (e.g., *Rhodospiridium toruloides*) or two different polypeptides (e.g., *Saccharomyces cerevisiae*) (2, 3).

Acyl carrier protein (ACP) is an indispensable component of both type I and type II FAS. It has a four-helix bundle fold, with a conserved serine that tethers a coenzyme-A derived 4'-phosphopantetheine moiety (4'-PP). The free sulfhydryl group of the 4'-PP arm anchors the growing acyl chain by a thioester bond. All type II ACPs can sequester the lengthening acyl chain deep into their hydrophobic core. The well-studied ones are *Escherichia coli*, spinach, *Plasmodium falciparum*, *Helicobacter pylori* (4–7), *Leishmania major* (8), and *Streptomyces coelicolor* (9). *E. coli* acyl-ACP crystal structures show that the aliphatic chain remains buried in the hydrophobic core, interacting with the side chain of hydrophobic residues lining the cavity. The labile thioester linkage between 4'-phosphopantetheine and the acyl chain also remains embedded in the cavity, and the terminal methyl group of the aliphatic-chain points toward the C-terminus of helix II and IV (4). Helix I, III, and the N-terminus of helix II move outward in C₁₀-EcACP, to accommodate the growing acyl chain (10). The conformation of butyryl (C₄-), hexanoyl (C₆-), and heptanoyl (C₇-) ACP structures lies between the unliganded and decanoyl (C₁₀)-ACP conformations (4, 10). Similarly, in spinach ACP, the backbone experiences a major conformational change to sequester the lengthening acyl chain (5). A switch-blade mechanism transfers the acyl chain from the hydrophobic cavity of ACP to the active site of the FAS enzymes (11). Acyl chain flipping has been observed in the crystal structure of *E. coli* ACP-FabA (fatty acid 3-hydroxyacyl-ACP dehydratase) cross-linked complex (12). Interestingly, the type II FAS enzymes can discriminate between acyl-ACP intermediates *via* allosteric interactions, even without flipping the acyl chain (13).

Type I ACP (metazoan) differs from type II in their overall surface charge and hydrophobicity. NMR studies on rat ACP demonstrate that the acylated forms do not experience significant chemical shift perturbations, suggesting lack of chain sequestration in the central cavity. Type I ACP also lacks the chain flipping mechanism. Instead, the phosphopantetheine-bound acyl chain remains buried within the grooves, present on its hydrophobic surface (14). *In silico* studies highlight the

[‡] These authors contributed equally to this work.

* For correspondence: Monica Sundd, monicasundd@ni.ac.in.

A GX_2GX_3G motif facilitates chain sequestration in yeast ACP

role of bulky hydrophobic residues present between helix II and III, *i.e.*, L2144, L2146, and V2174 in locking the ACP in a closed state. The modular and compact organization of reaction centers in type I FAS probably obviates the need for acyl chain sequestration (1).

Fungal FAS type I complex (PDB 2UV8) is remarkably different from the rat/pig type I system (PDB 2VZ8) in its overall size and architecture, revealed by crystallography and cryo-EM studies (2, 15). In addition to the canonical ACP fold, its ACP domain contains a four-helix subdomain that stabilizes the ACP structure. This class of type I ACP can sequester acyl chains as long as decanoyl (2, 16). The mechanism underlying acyl chain sequestration by fungal ACP and the delivery of acyl cargo to the cognate enzymes is not yet well understood. Progress in elucidating the same has been limited due to the large ACP didomain size (~20 kDa) and short shelf life of the intermediates.

Furthermore, fungal *FAS2* gene product has been recognized as a candidate target for drug intervention in *Candida parapsilosis* and *Candida albicans*. The microorganism depends on fatty acids for growth and virulence (17, 18). In view of the rising number of invasive fungal infections in immunosuppressed patients, and the emerging problem of drug resistance, it is necessary to study fungal FAS domains at the molecular level. *S. cerevisiae* is a widely accepted model to understand lipid metabolism in eukaryotes. Multiple X-ray (PDB 2UV8, 6QL9) and cryo-EM structures (PDB 6U5U, 6TA1) are available for its FAS complex (2, 15). NMR assignments of its ACP domain have also been published (19). Therefore, we have used *S. cerevisiae* ACP as a prototype, to understand acyl chain sequestration by fungal FAS. Our studies uncover a unique arrangement of glycine's in helix II and a threonine in helix IV that play crucial role in acyl chain sequestration. Moreover, we have identified the hydrophobic cavity of *ScACP* that sequesters the growing acyl chain.

Results

S. cerevisiae acyl carrier protein (*ScACP*) comprises two subdomains, (a) a canonical ACP domain (Ala138-Gly219) homologous to most type I and type II ACPs, and (b) a structural domain (Ala220-Leu302) found in fungi and a few bacterial species. Figure 1A shows a ribbon representation of the *ScACP* didomain obtained from the full-length FAS structure (PDB 2UV8). The NMR structure of *ScACP* is also available, PDB 2ML8 (16). In both the structures, the ACP subdomain (colored blue in Fig. 1A) comprises helices I–IV, and the structural domain is formed by helices V–VIII (colored cyan). The ACP subdomain has a four-helix bundle fold, similar to the type I ACP of rat (PDB 2PNG) and type II ACP of *E. coli* (PDB 1T8K), shown in Figure 1, B and C. The $\alpha 1$ – $\alpha 4$ helices of *ScACP* are analogous to the four helices of other type I and type II ACP (2). *ScACP* helix III displays a turn between Lys 200 and Thr 204, $i + 4$ residues apart in the solution structure (PDB 2ML8) (16). VADAR identified a backbone hydrogen bond at the same position in the crystal structure (2UV8), though Figure 1A generated using Chimera does not display a

helical turn in that region (20, 21). Figure 1D shows the multiple sequence alignment of *ScACP* subdomain with *C. albicans*, *R. norvegicus*, *E. coli*, and *P. falciparum* ACP. The conserved DSL motif of most type I and II ACPs is substituted with a KST sequence in *ScACP*. Met 44 of type II ACP is replaced with a Gly, and $^{44}\text{MALEEEFDTE}^{53}$ helix II sequence of *E. coli* ACP corresponds to a unique glycine rich motif $^{188}\text{GDLGKEFGTT}^{197}$ of *ScACP*. Residue numbering used in this study is in accordance with the available NMR (PDB 2ML8) and crystal structures (2UV8) (1, 16).

Acylation-induced chemical shift perturbations of *ScACP* are characteristic of chain sequestration

Uniformly labeled [$^1\text{H}^{15}\text{N}^{13}\text{C}$] apo-*ScACP* didomain (Ala 138-Leu 302) was enzymatically converted into various acyl-intermediates using its cognate 4'-phosphopantetheinyl transferase *ScPPT* (UNP P19097, Asn 1755-Gln 1877) and the respective acyl-coenzyme A. Conversion of the apo-form to the acyl-intermediate was confirmed by (a) native-PAGE, as the acylated form migrates ahead of apo-*ScACP* due to a higher negative charge, (b) molecular mass determined by electrospray ionization–mass spectrometry (ESI-MS), and (c) perturbations at the amides of Lys 179, Gln 183, and Asn 184 in a $^1\text{H}^{15}\text{N}$ HSQC spectrum, the hallmark of apo-to holo-*ScACP* conversion. Holo-*ScACP* chemical shifts were assigned based on the BMRB ID 16085 (19). C_4 - (δC_4 - δHolo -), C_{14} - (δC_{14} - δHolo -), and C_{16} -*ScACP* (δC_{16} - δHolo -) $^1\text{H}^{15}\text{N}$ HSQC spectra can be fully superimposed on the holo-*ScACP* spectra, suggesting lack of chain sequestration (data not shown). In contrast, C_8 - (δC_8 - δHolo -), C_{10} - (δC_{10} - δC_8 -), and C_{12} -*ScACP* (δC_{12} - δC_{10} -) amides displayed significant perturbations in both proton (^1H) and nitrogen (^{15}N) dimension. The two nuclei report very different interactions/changes. Proton chemical shifts are influenced by hydrogen bonds, inductive effects, and ring current effects, while nitrogen chemical shifts report secondary structure perturbations, changes in dihedral angles and hydrogen bonds of the preceding carbonyl (22, 23). Therefore, we have reported acylation-induced *ScACP* perturbations separately for ^1H and ^{15}N nuclei.

Figure 2, A and B display a plot for the changes in ^1H and ^{15}N chemical shift of dodecanoyl-*ScACP* (δC_{12} - δHolo -) as a function of residue number. Changes in ^1H chemical shift were observed for Gln 183, Asp 189, Gly 191, Glu 193, Gly 195, Thr196, Glu 199, Ala 210-Phe 217, and Ser 225, shown in Figure 2A. One standard deviation has been used as a cutoff to demarcate significant change. The residues displaying significant perturbation are localized in helix II, loop II, and helix IV, shown as swellings of the worm in Figure 2E. The magnitude of chemical shift change is directly proportional to the thickness of the worm. Nitrogen chemical shift changes were observed for Gly 188, Asp 189, Gly 191, Phe 194-Thr 196, Glu 199, Glu 202, Glu 207, Thr 212, Phe 213, Thr 216, Gly 222, and Ser 225. Several of these amides overlap with the ones displaying ^1H perturbations. The aforementioned residues are present in helix II, loop II, and helix IV, illustrated in Figure 2F. Figure 3A displays a multiple overlaid $^1\text{H}^{15}\text{N}$ HSQC spectra

A GX₂GX₃G motif facilitates chain sequestration in yeast ACP

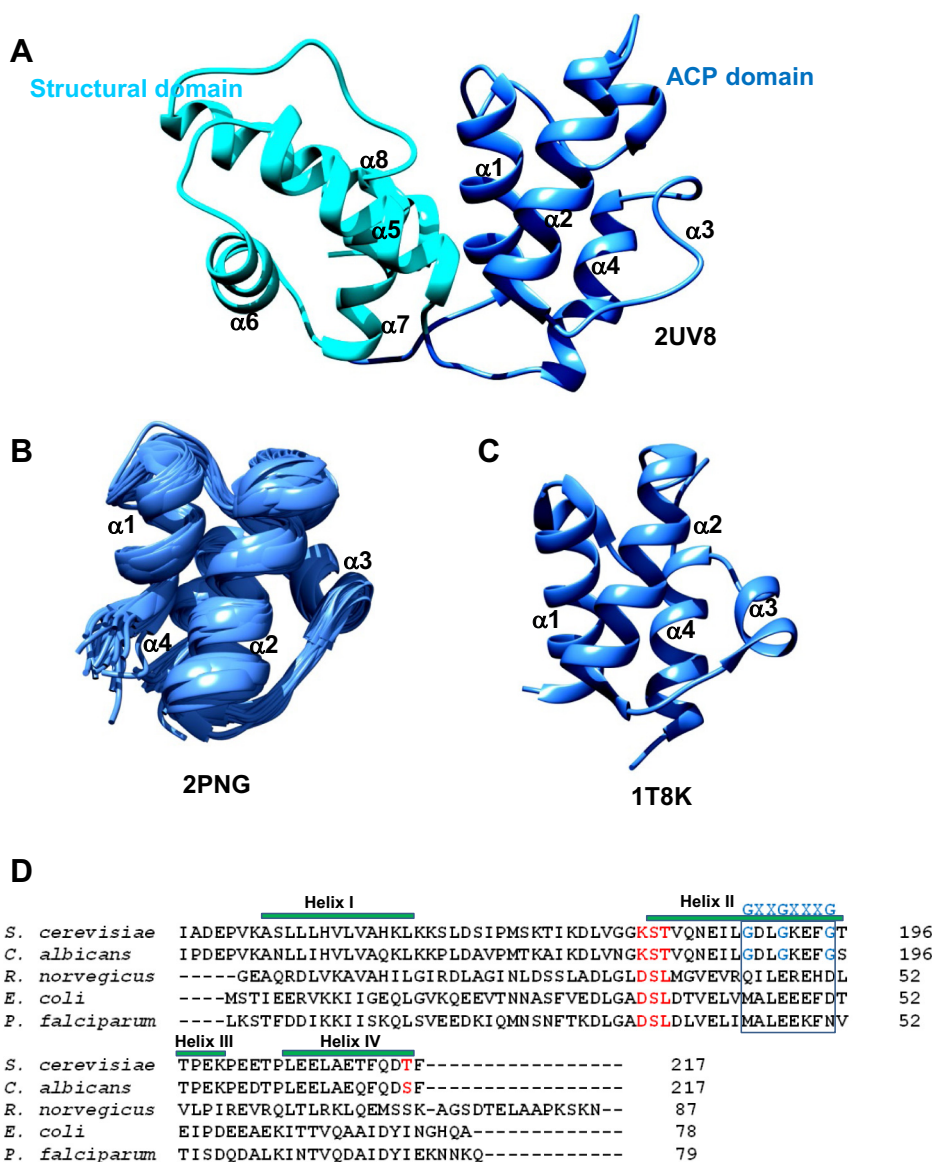


Figure 1. The ACP subdomain of ScACP is homologous to other type I and type II ACPs. A ribbon diagram of (A) ScACP didomain, displaying the ACP subdomain blue, and the structural domain cyan. B, type I ACP of rat (PDB 2PNG, lowest 20 NMR models), and (C) type II ACP of *E. coli* (PDB 1T8K), shown as ribbons. The figure was prepared using UCSF-Chimera (21). D, sequence comparison of ScACP (ACP subdomain) with other type I and type II ACPs. A GX₂GX₃G sequence is indicated by a blue box, conserved only in *Saccharomyces* and *Candida* spp. Sequence alignment was done using Clustal omega (<https://www.ebi.ac.uk/Tools/msa/clustalo>).

for holo-ScACP and its intermediates. Change in peak position of Gly188, Gly191 and Gly195 amide is shown. Thr 212 and Thr 216 peaks shifts in the intermediates are illustrated in Figure S1, A and B, respectively. The direction of chemical shift change is indicated by a forward pointing arrow. Holo peaks are colored red, C₈- blue, C₁₀- green, and C₁₂-ScACP magenta. Same color coding has been used throughout for all the spectra reported in the study. The molecular mass of apo-, holo-ScACP and acyl intermediates was determined using ESI-MS (Fig. S2, A–F). The observed mass in each case was within ±1 Da of the expected value.

Figure S3 shows the weighted-average amide chemical shift changes of C₈- (δC₈-δHolo-), C₁₀- (δC₁₀-δC₈-), and C₁₂- (δC₁₂-δC₁₀-) ScACP. The average amide chemical shift perturbations (ΔδAve_{H_N}) were calculated using Equation 1,

described under Experimental procedures. The ΔδAve_{H_N} changes have been mapped to a worm figure as well (Fig. S3, D–F). Notably, C₈-ScACP displayed perturbations primarily in helix II and loop II (Fig. S3, A and D). C₁₀- ScACP induced changes in helix II, loop II, and helix IV (Fig. S3, B and E). C₁₂-ScACP formation was accompanied with large magnitude chemical shift changes of helix II, loop II, and helix IV amides (Fig. S3, C and F).

Chemical shift changes >1SD were also observed at the carbonyls of several residues of C₁₂-ScACP. Val 176, Leu187, Gly 188, Leu 190, Phe 194, Pro 198, Pro 201, Thr 212, Phe 213, Gln 214, Asp 215, Thr 217, and Leu 221 displayed significant change (Fig. 2C). The aforementioned residues are localized in helix II, loop II, and helix IV, as shown in Figure 2G. Perturbations are shown as swelling of the ScACP worm diagram.

A GX_2GX_3G motif facilitates chain sequestration in yeast ACP

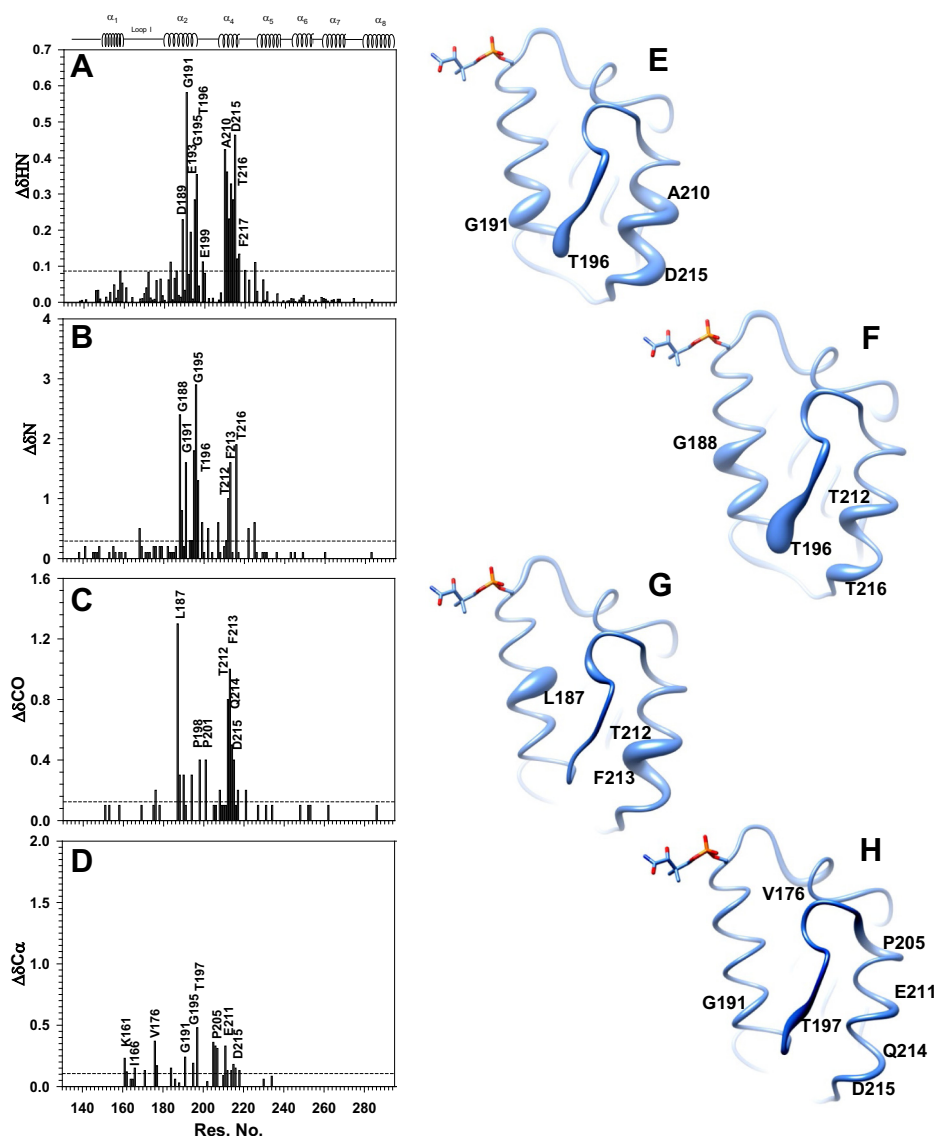


Figure 2. Chemical shift perturbations suggest C_{12} -chain sequestration by ScACP. Changes in the backbone (A) amide proton, (B) nitrogen, (C) carbonyl, and (D) $C\alpha$ chemical shift of ScACP upon C_{12} -intermediate (δC_{12} - δ Holo-ScACP) formation. A worm representation of ScACP, displaying the changes in amide (E) proton, (F) nitrogen, (G) carbonyl, and (H) $C\alpha$ chemical shift as swellings. In each case, the thickness of the worm is directly proportional to the magnitude of chemical shift change. The figure was prepared using UCSF-Chimera (21).

Figure S1, C–F display superimposed HNC0 spectra for Leu187, Phe 194, Thr 212, and Asp 215, respectively. Large upfield changes were observed for Leu 187 carbonyl (~ 1.35 ppm), Thr 212 (~ 0.8 ppm), and Phe 213 (~ 1.0 ppm). Solid-state NMR studies have previously shown that the chemical shift of a hydrogen-bonded amide proton or carbonyl displays magnetic deshielding with the decrease in $R_{N\dots O}$ distance (24–26). Thus, the upfield change in the carbonyl chemical shift of the abovementioned residues indicates lengthening of their associated backbone hydrogen bonds.

$C\alpha$ chemical shift changes of C_{12} -ScACP (δC_{12} - δ Holo-) were also followed as a function of residue number, illustrated in **Figure 2D**. Residues displaying $C\alpha$ chemical shift change have been mapped to the ScACP worm structure in **Figure 2H**. Overall, the observed $C\alpha$ changes were relatively small, primarily in helix II and loop II residues, consistent with a previous NMR study (16).

Taken together, the unique pattern of acyl-ScACP perturbations, observed simultaneously in helix II, loop II and helix IV, is a hallmark of chain sequestration.

TALOS+ predicts small changes in the dihedral angles of helix II, loop II, and helix IV of C_{12} -ScACP

1H , ^{15}N , ^{13}CO , and $^{13}C\alpha$ chemical shifts were used to predict dihedral angles of holo- and C_{12} -ScACP using TALOS+ (27). **Figure 4A** displays a plot for the Φ , ψ angles of holo-ScACP and its dodecanoyl- form, as a function of residue number. In the figure, black filled circles represent Φ angles and yellow triangles ψ angles for wild-type ScACP. C_{12} -ScACP Φ angles are shown by red filled circles and ψ angles by green triangles. A dotted line separates the Φ and ψ angles. As illustrated in the figure, several residues present in helix II, loop II, and helix IV displayed minor changes in dihedral

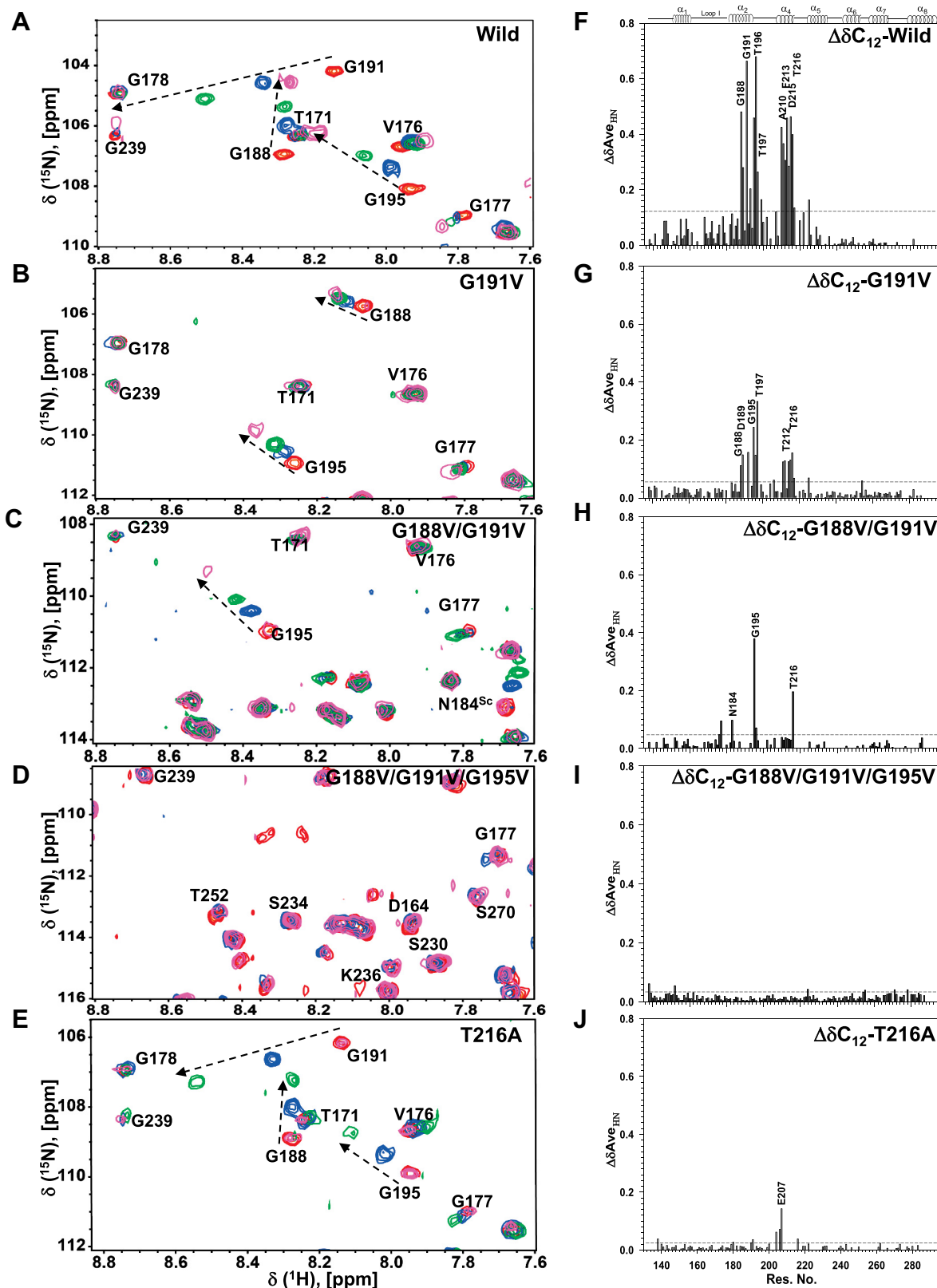


Figure 3. A GX_2GX_3G motif in helix II and a threonine in helix IV are necessary for acyl chain sequestration. Multiple overlaid 1H - ^{15}N HSQC spectra for (A) Wild, (B) G191V, (C) G188V/G191V, (D) G188V/G191V/G195V, and (E) T216A ScACP, displaying Gly 188, Gly 191, and Gly 195 peaks. Holo-peaks are colored red, C_8 - blue, C_{10} - green, and C_{12-} - magenta. Weighted average amide chemical shift changes observed upon formation of C_{12-} intermediates of (F) Wild, (G) G191V, (H) G188V/G191V, (I) G188V/G191V/G195V and (J) T216A ScACP. For the triple mutant G188V/G191V/G195V, ^{15}N TROSY-HSQC spectra were acquired as it gave better signal. One standard deviation is shown as a discontinuous horizontal line. $\Delta\delta_{ave\ H_N}$ chemical shifts were calculated using Equation 1.

A GX_2GX_3G motif facilitates chain sequestration in yeast ACP

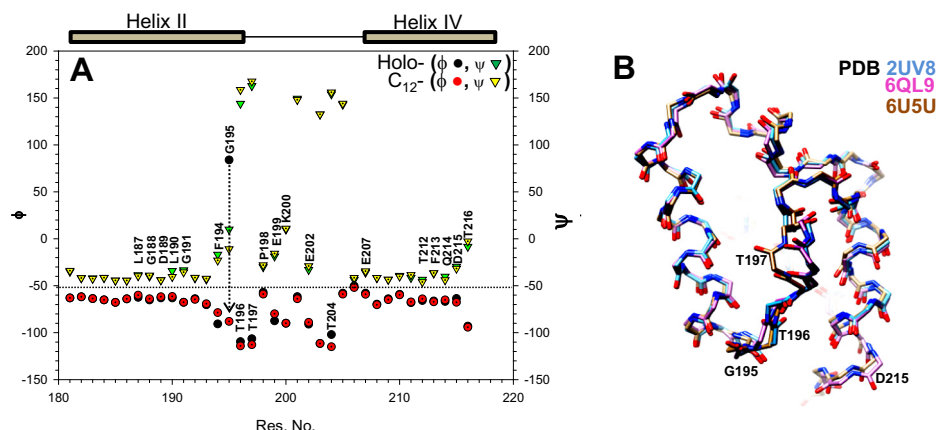


Figure 4. TALOS+ predicts minor dihedral angle changes in helix II, loop II and helix IV. *A*, a plot of backbone dihedral angles as a function of residue number. The Φ, Ψ angles for holo-ScACP are represented by black filled circles and inverted green triangles, while the symbols for the Φ, Ψ angles of C_{12} -ScACP are red filled circles and yellow inverted triangles, respectively. *B*, overlay of the ScACP didomain backbone in the PDB structures 2UV8 (cyan), 6QL9 (pink), and 6U5U (brown).

angles, suggesting slight alteration of the backbone conformation. Though most of the changes are relatively small, added together they may induce a significant change in the size of the hydrophobic cavity. Notably, Gly 195 displayed a large change in its Φ angle in C_{12} -ScACP compared with wild-ScACP. Using VADAR, we measured the Φ, Ψ dihedral angles of Gly 195 in the crystal structure PDB 2UV8 ($92^\circ, -43^\circ$) and the NMR structure 2ML8 ($75.3^\circ, -18^\circ$). These values are comparable to the holo-ScACP dihedral angles determined (84° and 10°) in the present study. However, in C_{12} -ScACP, a noticeable change was observed (-88° and 11°), suggesting a 180° flip of the Gly 195 backbone. These TALOS+ predictions were substantiated by ScACP crystal (2UV8, 6QL9) and cryo-EM structure (6U5U), where Gly 195 and other loop II residues display a remarkably different conformation (Fig. 4B).

Helanal-Plus detects large bending angles in helices II and IV

Three glycines present within a $^{188}GX_2GX_3G^{195}$ motif of helix II displayed significant perturbations in C_{12} -ScACP. Glycine has been shown to induce kinks in helices. Therefore, Helanal-Plus server was used to predict bending angles in the crystal structure PDB 2UV8 (28). Local bending angles were calculated from the helix axes fitted to the C_α atoms of residues $(i - 3) - i$ and $i - (i + 3)$. Table 1 lists the bending angles for helices II and IV of holo-ScACP determined using Helanal-Plus. Both the helices displayed slight distortions in their axes. A bending angle of $\sim 10^\circ$ was observed for the axes fitted to Glu185 Gly188 Gly188 Gly191 and 11° for Gly188 Gly191 Gly191 and Phe194, in helix III. Similarly, in helix IV, a bending angle of 13.6° was observed for the axes fitted to Leu209 Thr212 Thr212 and Asp215. These bending angles are less than 20° and therefore pro-kink. However, they might transform into a kink under certain functional conditions.

VADAR identifies long/broken hydrogen bonds in helix II and IV

Backbone hydrogen bonds were calculated for the ScACP didomain, PDB 2UV8 using VADAR (Volume Area Dihedral

Angle Reporter), listed in Table 2 (20). In helix II, Leu187CO-NGly191 hydrogen bond is longer than average, $\sim 2.8 \text{ \AA}$. In helix IV, several longer than average hydrogen bonds were identified; Glu208 CO-NThr212 is 2.9 \AA , while Glu 211CO-NAsp215 and Thr212CO-NThr216 could not be detected by VADAR. The corresponding CO-N distances were measured manually using Chimera, $\sim 2.7 \text{ \AA}$ and 3.4 \AA , respectively (21).

$^{188}GX_2GX_3G^{195}$ sequence is necessary for acyl chain sequestration

To uncover the role of the $^{188}GX_2GX_3G^{195}$ motif in ScACP function, Gly 188, Gly 191, and Gly 195 were singly mutated to valine. A G188V/G191V (double mutant), as well as G188V/G191V/G195V (triple mutant), was also generated. Figure S4, A-C and F-H show changes in the 1H and ^{15}N chemical shift upon mutagenesis in G188V, G191V, and G195VScACP. Perturbations were observed primarily near the site of mutation, suggesting no major change in the overall fold.

Figure 3, B-D show regions of multiple overlaid $^1H^{15}N$ HSQC spectra for holo-, C_8 -, C_{10} -, and C_{12} -intermediates of G191V, G188V/G191V, and G188V/G191V/G195V, respectively. Figure 3G shows a histogram for the average amide

Table 1
Bending angles calculated from local helix axes fitted to CA atoms $((i - 3) - i)$ and $(i - (i + 3))$ using Helanal-Plus (28)

Res. (i - 3)	Res. i	Res. i	Res. (i + 3)	Bending angle ($^\circ$)
180 S	183 Q	183 Q	186 I	5.6
181 T	184 N	184 N	187 L	2.9
182 V	185 E	185 E	188 G	2.4
183 Q	186 I	186 I	189 D	4.7
184 N	187 L	187 L	190 L	8.5
185 E	188 G	188 G	191 G	10.2
186 I	189 D	189 D	192 K	8.4
187 L	190 L	190 L	193 E	9.5
188 G	191 G	191 G	194 F	11.2
206 L	209 L	209 L	212 T	3.5
207 E	210 A	210 A	213 F	8.4
208 E	211 E	211 E	214 Q	6.4
209 L	212 T	212 T	215 D	13.6
210 A	213 F	213 F	216 T	8.3

Helix IV as represented in bold.

Table 2
Backbone hydrogen bonds in helix II and IV of ScACP, (PDB 2UV8) calculated using VADAR (20)

H Bond acceptor (CO)	H Bond donor (N)	O-N distance Å	Type
Thr 181	Glu 185	2.36, 2.34, 2.33	i, i + 4
Val 182	Ile 186	2.35, 2.34, 2.36	i, i + 4
Gln 183	Leu 187	2.21, 2.18, 2.20	i, i + 4
Asn 184	Gly 188	2.32, 2.29, 2.28	i, i + 4
Glu 185	Asp 189	2.07, 2.07, 2.09	i, i + 4
Ile 186	Leu 190	2.39, 2.43, 2.41	i, i + 4
Leu 187	Gly 191	2.80, 2.80, 2.81	i, i + 4
Gly 188	Lys 192	2.56, 2.59, 2.58	i, i + 4
Asp 189	Glu 193	2.63, 2.63, 2.62	i, i + 4
Leu 190	Phe 194	2.04, 2.03, 2.07	i, i + 4
Gly 191	Gly 195	2.34, 2.31, 2.36	i, i + 4
Leu 206	Ala 210	2.11, 2.10, 2.08	i, i + 4
Glu 207	Gly 211	2.54, 2.56, 2.54	i, i + 4
Glu 208	Thr 212	2.92, 2.90, 2.87	i, i + 4
Leu 209	Phe 213	2.10, 2.10, 2.10	i, i + 4
Ala 210	Gln 214	2.37, 2.39, 2.39	i, i + 4
Glu 211	Asp 215	Long	i, i + 4
Glu 211	Gln 214	2.60, 2.57, 2.55	i, i + 3
Thr 212	Thr 216	Long	i, i + 4
Phe 213	Phe 217	2.63, 2.57, 2.59	i, i + 4

The three H bond length values correspond to chains A, B, and C in the crystal structure (PDB 2UV8). Helix IV as represented in bold.

chemical shift changes ($\Delta\delta A_{veHN}$) of G191VScACP upon conversion to its C₁₂-intermediate ($\delta C_{12}-\delta_{holo-}$). A remarkable decrease in the magnitude of chemical shift change was observed in C₁₂-G191VScACP (single mutant), compared with C₁₂-wild type ScACP. C₁₂-G188V/G191VScACP (double-mutant) sample also displayed a decrease in the magnitude of chemical shift change (Fig. 3, C and H). In the triple-mutant G188V/G191V/G195VScACP, the ¹H¹⁵N HSQC spectra of C₈⁻ (blue), C₁₀⁻ (green), C₁₂⁻ (magenta), and holo-form (red) overlapped completely (Fig. 3D). $\Delta\delta A_{veHN}$ chemical shift perturbations were insignificant (Fig. 3I), suggesting complete loss of chain engulfment in the G188V/G191V/G195VScACP cavity (Fig. 3F). The chemical shift of Gln 183 and Asn184 amides corroborated the conversion of apo-to C₁₂-ScACP. The molecular mass of all the intermediates was confirmed by ESI-MS. Due to the hydrophobic nature of the triple mutant, obtaining good-quality ESI-MS spectra for the fully converted C₁₂-triple mutant was a challenge. We were able to obtain ESI-MS spectra for the half-converted C₈⁻-G188V/G191V/G195VScACP (Fig. S2G). Two species could be identified, (a) C₈⁻-form (18,615 Da), and (b) apo-form (18,203 Da), confirming the formation of triple mutant intermediates.

Hydrolysis of the C₁₂-chain was followed in wild type, G191V, G188V/G191V, and G188V/G191V/G195VScACP dodecanoyl intermediates as a function of time. This was done by acquiring a series of ¹H¹⁵N HSQC spectra at 298 K. As illustrated in Figure 5A, Thr216 HN has a chemical shift of 106 ppm in wild-type C₁₂-ScACP. In a freshly prepared C₁₂-wild-type sample, C₁₂-Thr216 conformer was 100% populated (Fig. 5A), while in the single mutant (C₁₂-G191V) 86% (Fig. 5B), and the double glycine mutant (G188V/G191V) displayed only 64% C₁₂-conformer (Fig. 5C). Over time, the samples hydrolyzed, and holo-peaks appeared at a nitrogen chemical shift of 104 ppm. In G188V/G191V/G195VScACP sample, only one conformer of Thr216 was visible right from the beginning, corresponding to

the holo-form, *i.e.*, at 104 ppm (Fig. 5D). Conceivably, C₁₂-G188V/G191V/G195VScACP gets hydrolyzed during sample preparation. Wild type C₁₂-ScACP sample was stable for >48 h, C₁₂-G191VScACP single glycine mutant ~15 h, C₁₂-G188V/G191VScACP double glycine mutant ~9 h, and G188V/G191V/G195VScACP (triple glycine mutant) 0 h. The stability of the C₁₂-intermediates was in the order wild-type > single > double > triple glycine mutant.

Thr 216 plays an important role in C₁₂-chain sequestration

Several threonines of helix IV displayed large perturbations in the acyl-ScACP intermediates. Helanal-Plus also predicted a partial bend at Thr 208 and Thr 212 in the ScACP structure, PDB 2UV8. To uncover the role of the two threonines in ScACP function, they were mutated to alanine. ¹H and ¹⁵N chemical shift changes of T212A and T216AScACP confirmed that the overall fold was retained in the mutant (Fig. S4, D, I, E and J).

Acylation-induced chemical shift perturbations of C₈⁻, C₁₀⁻, and C₁₂-T212AScACP were similar to wild-type ScACP (data not shown). However, T216AScACP displayed a remarkable change in sequestration. Figure 3E shows the multiple overlaid ¹H¹⁵N HSQC spectra for holo-, C₈⁻, C₁₀⁻, and C₁₂-T216AScACP (Fig. 3E). Significant chemical shift perturbations were observed for C₈⁻ and C₁₀⁻-T216AScACP. However, peaks for C₁₂-T216AScACP displayed insignificant change (Fig. 3J). The ¹H¹⁵N HSQC spectra of C₁₂-T216AScACP fully overlapped with its holo-T216AScACP, suggesting complete hydrolysis of the C₁₂-chain. The molecular mass of C₁₂-T216AScACP was confirmed by ESI-MS (Fig. S2H). The three samples C₁₂-T212A, C₁₂-T216A, and C₁₂-wildScACP were prepared simultaneously, using the same ScPPT, C₁₂-CoA, and buffer stocks.

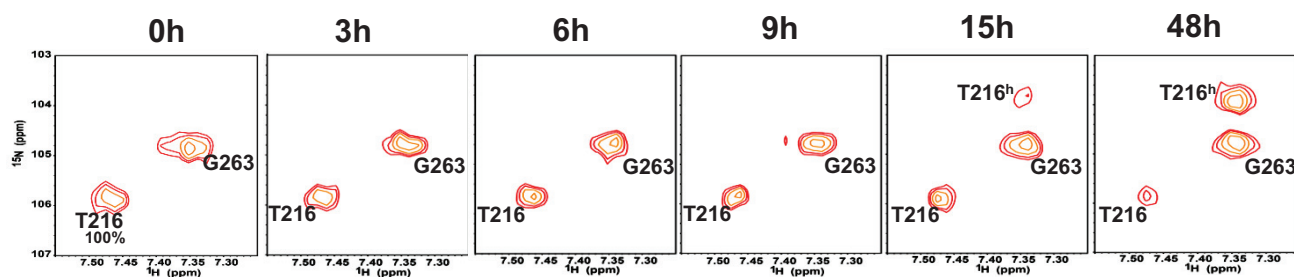
¹H¹⁵N HSQC spectra of holo-, C₈⁻, and C₁₀⁻-intermediates of T216AScACP were compared to wildScACP intermediates. The change in the chemical shift of holo-ScACP upon conversion to C₈⁻ and C₁₀⁻-wildScACP is indicated by a black arrow, and T216AScACP by a red arrow (Fig. S5). Interestingly, most C₁₀-T216AScACP residues (green peaks) displayed larger perturbations compared with C₁₀-wild type ScACP (green peaks), shown in Figure S5, A–C. However, the C₈⁻-peaks of the two proteins (colored blue) were similar/comparable. Large magnitude changes of C₁₀-T216A peaks probably reflect reduction in the overall size/capacity of the hydrophobic cavity upon mutation of Thr216 to Ala.

The opening of the hydrophobic cavity of ScACP lies between helix II and loop II

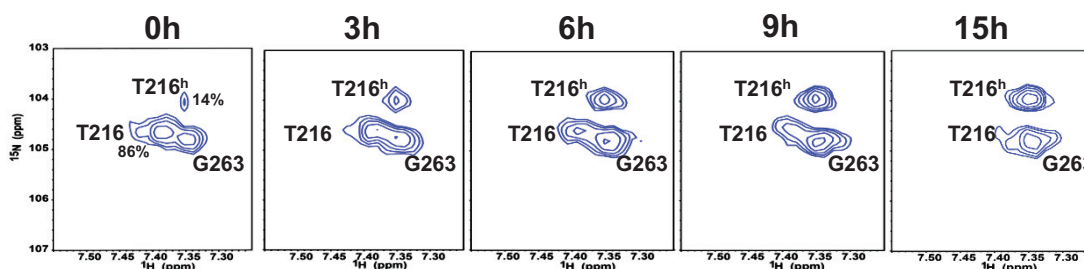
CastP (Computed Atlas of Surface Topography of Proteins) 3.0 server (29) was used to identify the cavities of ScACP didomain in the crystal structure 2UV8. A total of 29 pockets were identified. As listed in Figure 6A, cavity #5 formed by Leu 187, Leu 190, Gly 191, Gly 195-Pro 198, Pro 201, Leu 209, and Phe 213 is in compliance with our C₈-ScACP chemical shift perturbation data and glycine mutagenesis studies. The opening of this cavity lies between helix II and loop II. The cavity is

A GX_2GX_3G motif facilitates chain sequestration in yeast ACP

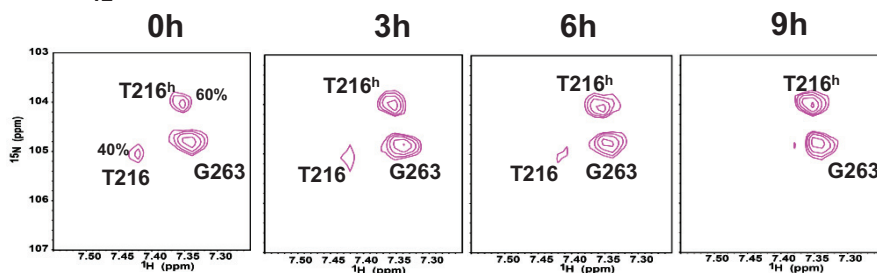
A C_{12} -WildScACP



B C_{12} -G191VScACP



C C_{12} -G188V/G191VScACP



D C_{12} -G188V/G191V/G195VScACP

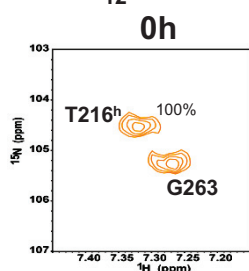


Figure 5. Mutation of glycines in the GX_2GX_3G motif increases the rate of acyl chain hydrolysis. $^1H^{15}N$ HSQC spectra displaying chemical shift changes of Thr216 HN peak in the C_{12} -intermediates of (A) holo-, (B) G191V, (C) G188V/G191V, and (D) G188V/G191V/G195VScACP. Thr216 peak hydrolyzes to the holo-form (T216^h) over a period of ~3 days in wild ScACP at room temperature.

present between the second and third turns of helix II, with Leu 187 and Gly 191 present at the mouth of the cavity (Fig. 6B). Notably, Leu 187 displayed large carbonyl chemical shift perturbations in our studies. We speculate that this is the opening of the primary hydrophobic cavity of ScACP, as residues forming this cavity (identified by CastP) displayed perturbations in all three intermediates, C_{8^-} , C_{10^-} , and C_{12^-} . Another hydrophobic cavity #12 observed at the base of ScACP is formed by

Phe 194, Phe 213, Thr 216, and Phe 217. This appears to be the second cavity that harbors the C_{12^-} chain (Fig. 6C), as the aforementioned amides displayed significant perturbations upon C_{12^-} -ScACP formation, and mutation of T216 led to the complete loss of C_{12^-} chain sequestration. Figure 6D shows the surface figure for the ScACP didomain (PDB 2UV8), displaying the opening of the cavity (shown by a downward pointing arrow). The ACP subdomain is shown as ribbons (Fig. 6D).

A GX_2GX_3G motif facilitates chain sequestration in yeast ACP

CastP calculated primary cavity size (volume between the walls) was $\sim 134 \text{ \AA}^3$, and the second cavity was $\sim 30 \text{ \AA}^3$. With the help of 3V software, we calculated the volume of the C_8 - and C_{10} -chains using PDB 2FAE (30). The calculated volume of C_8 -chain was 154 \AA^3 , and C_{10} -chain approx. 186 \AA^3 . For the C_{12} -chain, PDB 2BYZ was used, and the calculated volume was $\sim 228 \text{ \AA}^3$.

Discussion

ACP is an essential cofactor, indispensable for fatty acid synthesis. All ACPs have a conserved four-helix bundle fold, but vary in their mechanism of function. Type I ACP does not sequester the acyl chain, while the type II ACP engulfs the acyl chain in their hydrophobic core. Fungal ACPs are an exception, as they share commonalities with both type I and type II ACP. *S. cerevisiae* ACP is a domain of a large complex and has a molecular surface similar to type I ACP. However, analogous to type II ACP, it can partially sequester the growing acyl chain in its hydrophobic core and transport it to the active site of the FAS enzymes (16). In the ScFAS structure, the phosphopantetheine arm was found flipped into the active site of the ketoacyl synthase domain, suggesting conservation of a

switchblade mechanism (2, 15). The molecular mechanism underlying acyl chain sequestration by ScACP and transfer to the FAS enzymes remains to be fully understood.

Our NMR chemical shift perturbation studies disclose the indispensable role of a $^{188}GX_2GX_3G^{195}$ motif in ScACP function. Considering chemical shift perturbations as a measure of chain sequestration, complete loss of sequestration was observed upon mutation of the three glycines in the sequence to valine. The G191V single and G188V/G191V double mutants displayed a remarkable decrease in the chain sequestration and faster release of the acyl chain. A previous bioinformatics study on membrane proteins has shown a close link between the GX_2GX_3G motif and helical kinks. Nearly 62% of the time, the sequence was observed near a glycine kink, and in 48% of the cases, it contained a kink center (31). Glycine can access a wide range of phi, psi torsion angles, and thereby introduce conformational flexibility in a helix. Glycine kink plays important role in the function of membrane proteins (32–36). In soluble proteins as well, namely PARK7 gene, encoding DJ-1, very long chain acyl CoA dehydrogenase, cellular retinol-binding protein, thermolysin, quorum sensing master regulator of *V. cholerae* HapR, and amyloid precursor protein, kinks/bends are important for function (37–44).

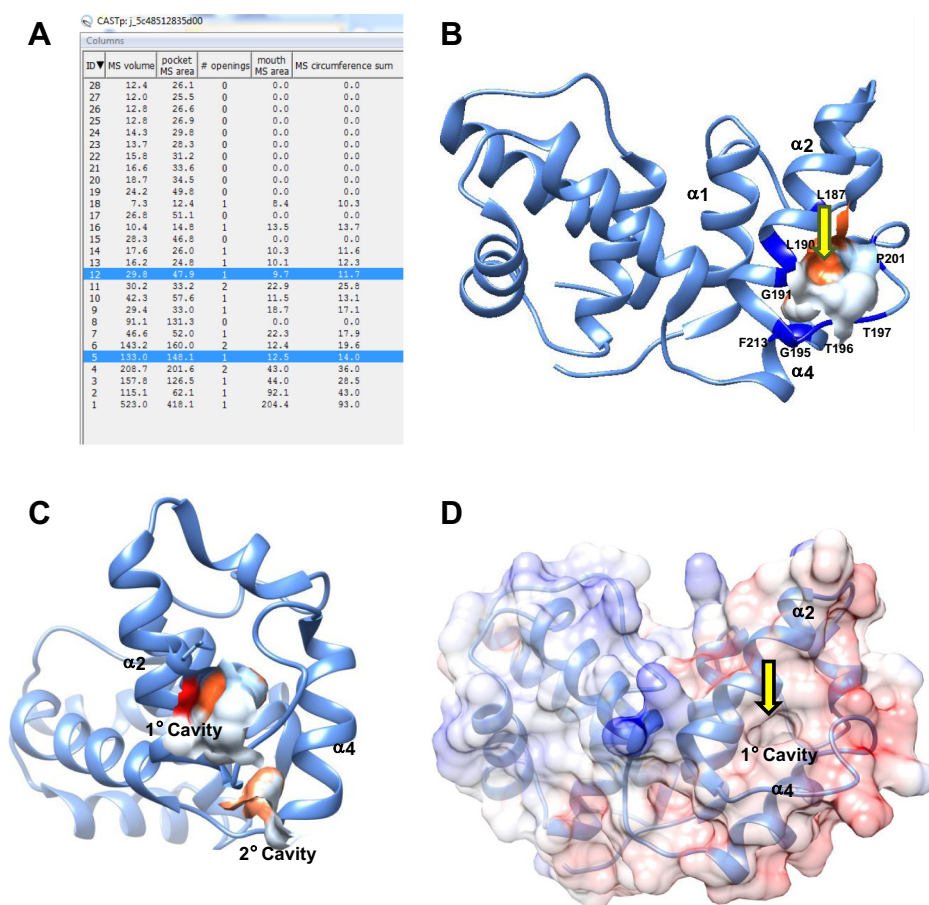


Figure 6. The hydrophobic cavity of ScACP didomain (PDB 2UV8) lies between helix II and IV. A, all 29 cavities predicted by CastP, based on the crystal structure of the didomain (PDB 2UV8). B, one of the cavities predicted by CastP #5, in compliance with NMR chemical shift perturbations appears to be the primary hydrophobic cavity. C, ScACP didomain, displaying the location of the primary (#5), and a second cavity (#12), present at the base of helix IV, identified based on NMR chemical shift perturbations. D, surface diagram of ScACP, colored based on coulombic charge. The opening of the primary cavity is shown by a downward pointing arrow.

A GX₂GX₃G motif facilitates chain sequestration in yeast ACP

ScACP too seems to rely on a glycine-rich ¹⁸⁸GX₂GX₃G¹⁹⁵ motif for its function. Several observations support this proposition; (a) significant amide and carbonyl chemical shift changes at the backbone of ¹⁸⁸GX₂GX₃G¹⁹⁵ sequence of helix II in the intermediates, (b) HELANAL-Plus predictions, suggesting a partial kink centred at Leu187 CO-HN Gly191 based on the crystal structure, (c) loss of acyl chain sequestration upon mutation of the three glycine in the ¹⁸⁸GX₂GX₃G¹⁹⁵ sequence to valine, and (d) faster release of the acyl chain in the glycine to valine mutants. All three glycines appear to contribute to function, as the absence of any one of them decreases the level of chain sequestration, but does not inhibit it completely. Chain protection decreased remarkably with the successive loss of glycine present in the GX₂GX₃G motif.

Interestingly, a helix IV residing threonine of ScACP governs sequestration of longer acyl chains. Threonine and serine both can form hydrogen bonds with the backbone of a nearby residue when present in a helical kink. The side chain -Oγ group of threonine competes with the backbone amide or carbonyl, forming an (i + 4) or (i + 3) intrahelical hydrogen bond, giving rise to a slight bend in the helix (45, 46). Ser/Thr-dependent helical kinks play important role in β₂-adrenergic receptor function and also in FcγRIIB (45, 47, 48). In ScACP as well, several observations reinforce the possibility of a threonine dependent kink; large chemical shift changes at Thr 212 and Thr 216 amides upon C₁₂ chain attachment, loss of C₁₂-chain sequestration upon mutation of Thr 216 to Ala, Helanal-Plus analysis predicting a partial bend centered at Thr 212 in helix IV, long hydrogen bonds involving Glu 211 and Thr 212 in helix IV, and upfield carbonyl chemical shift changes of Thr 212 and Asp 213 in the C₁₂-intermediate. Based on the crystal structure 2UV8, both helix II and IV of holo-ScACP are pro-kink. Carbonyl chemical shift changes suggest lengthening of the backbone hydrogen bonds near these bends upon acyl chain sequestration. We speculate that the bends intensify in the intermediates, resulting in outward movement of the post kink regions of helix II and IV, expanding cavity size, and thereby generating additional space for the acyl chain.

Combining chemical shift perturbation data with CastP analysis, we have identified the hydrophobic cavity of ScACP (PDB 2UV8) that harbors the growing acyl chain. Considering chemical shift perturbation as footprints of chain sequestration, the path traversed by the acyl chain in the cavity has been fully traced. A large cavity located near the ¹⁸⁸GX₂GX₃G¹⁹⁵ sequence of helix II and loop II is the primary cavity. The attachment of C₈-chain induces perturbations in the residues lining this cavity. A smaller second cavity identified at the base of helix IV is surrounded by residues that display perturbations in C₁₀- and C₁₂-intermediates. Thus, C₈-chain is sequestered in the primary cavity, while longer acyl chains require primary as well as the second cavity. Comparing cavity size and chain volume, at least 15% expansion of the primary cavity would be required to sequester the C₈-chain. C₁₀-chain would require a total of 30%, and C₁₂-chain 40% increase in volume of the primary and second cavity combined together. Mutagenesis studies underscore the role of three helix II residing glycine, and a helix IV localized threonine in bringing about this

change. In the absence of either of the residues, ScACP acyl chain protection is compromised.

Altogether, this is the first report that offers novel insights into the hydrophobic cavity of ScACP, and its unique mechanism of expansion. ScACP functions by virtue of distortions in helix II and IV that intensify upon acyl chain elongation. The conformational change induced by glycine and threonine kinks generates space to accommodate the lengthening acyl chain. For shorter chains (C₈-), helix II perturbations are sufficient. Longer acyl chains (C₁₀- and C₁₂-) require the second helix to undergo a sizeable change as well. The location of the hydrophobic cavity at the carboxyl-end of helix II and IV, and its opening at an unusual position between the second and third turns of helix II, highlights unique differences between the mechanism of function ScACP and type II ACP. The overrepresentation of glycine and threonine in ScACP is a feature of membrane proteins and for the first time being reported to play a role in ACP function.

Experimental procedures

Cloning, expression, and purification

S. cerevisiae ACP (ScACP, Ala138-Leu302) and its phosphopantetheinyl transferase (ScPPT, Asn1755-Gln1877) are present as domains of FAS alpha subunit (UNP P19097). The corresponding segments of the FAS gene were cloned separately in two pET28a vectors. Mutations in the ACP subdomain were generated by site-directed mutagenesis, using Phusion enzyme (Thermo Scientific). The plasmid was transformed in *E. coli* BL21 Rosetta cells. Single colonies were inoculated in 5 ml LB medium and grown overnight. The cultures were transferred to 1 l uniformly labeled [¹H, ¹⁵N, ¹³C] M9 minimal media, containing 1 g/l ¹⁵NH₄Cl and 2 g/l ¹³C glucose. Expression of the protein was induced with 1 mM IPTG at 25 °C, for 14 to 16 h. Cells were harvested by pelleting and the lysate subjected to sonication, followed by resuspension in 20 mM Tris-HCl, pH 7.5, 100 mM NaCl. The sample was centrifuged and the supernatant loaded on a Ni²⁺-NTA chromatography column. The bound protein was eluted with 50 to 250 mM Imidazole, followed by a Superdex 200 HiLoad 16/60 size-exclusion chromatography column.

ScPPT assay

Enzyme assays were performed in 2 ml volume (20 mM Tris-HCl, pH 7.5, 100 mM NaCl, 10 mM MgCl₂), with unlabeled or uniformly labeled [¹H, ¹⁵N, ¹³C] 20 μM ScACP, 1 to 5 μM ScPPT, and 60 μM acyl-Coenzyme A. Assays were incubated for 2 h, at 37 °C. Reaction product was qualitatively analyzed on a 10% Native-PAGE and quantitatively by ESI-MS (Thermo Scientific Orbitrap). All glycine to valine mutants, namely G188V, G191V, G195V, double mutant (G188V/G191V), and the triple mutants (G188V/G191V/G195V) ScACP required higher ScPPT concentration (20–30 μM) for full conversion.

ESI–mass spectrometry

The assay samples were passed through C₄ Zip Tips to remove salt and the final sample eluted in 50 to 80% acetonitrile, 0.1% trifluoroacetic acid for analysis in ESI-MS (Orbitrap, Thermo Scientific). The expected molecular mass of apo-ScACP was 18,023 and holo-18,363 Da.

NMR sample preparation and data acquisition

NMR samples for ¹H¹⁵N comprised 0.3 to 0.5 mM acyl-ACP and ~1 mM for triple resonance experiments, 20 mM Tris-HCl pH 7.5, 100 mM NaCl, 10% D₂O, and 0.5% Sodium Azide. Two- and three-dimensional NMR experiments, namely ¹H¹⁵N HSQC, HNCACB, CBCAcoNH, CCcoNH, HNcoCA, and HNCA, were acquired on a Bruker Avance III 700 MHz NMR spectrometer, equipped with a TXI probe, installed at the National Institute of Immunology, New Delhi, India. Experiments were performed at 298 K throughout. NMR data were processed on a workstation running Red Hat Enterprise Linux 5.0, using NMRPipe/NMRDraw (49). The data were multiplied by a phase-shifted sinebell apodization function in all dimensions and analyzed using Sparky (50).

¹H¹⁵N HSQC spectra were acquired using 1024 data points (t₂) dimension and 512 data points (t₁) dimension. CBCA-coNH, HNCACB, CCcoNH experiments were collected with 1024 (t₃) × 128 (t₁) × 32 (t₂) complex data points. Data were linear predicted in the forward direction for up to half the number of experimental points in the indirect dimension. ¹⁵N¹³C spectra were referenced indirectly using sodium 2, 2-dimethyl-2-silapentane-5-sulfonate (DSS) as a chemical shift standard (51).

Data analysis

Changes in the amide chemical shift for the mutant proteins have been reported as weighted average chemical shift ($\Delta\delta_{\text{Ave}}$), using equation (52)

$$\Delta\delta_{\text{Ave}} = [(\Delta\delta_{\text{HN}})^2 + (\Delta\delta_{\text{N}}/5)^2]^{1/2} \quad (1)$$

Here, $\Delta\delta_{\text{NH}}$ and $\Delta\delta_{\text{N}}$ denote chemical shift change in the proton and nitrogen dimension, respectively. A standard deviation of ± 1 has been used as a cutoff and represented by the horizontal line in the figures.

Data availability

All data are available from the authors upon request. Please send request to Monica Sundd, monicasundd@nii.ac.in.

Supporting information—This article contains supporting information.

Acknowledgments—Authors thank the Department of Biotechnology (D.B.T.), Govt. of India for infrastructure and financial support. University Grants Commission, Govt. of India is duly acknowledged for providing fellowship to U. Y. The authors are grateful to Ms Shanta Sen, Mass Spectrometry facility, NII for

helping with ESI-MS data. Our sincere thanks to Prof. Sneha Sudha Komath, SLS, JNU, for providing us the *S. cerevisiae* genome.

Author contributions—Garima and M. S. conceptualization; Garima and R. P. data curation; Garima and M. S. formal analysis; Garima. investigation; M. S. supervision; M. S. validation; M. S. visualization; U. Y. and M. S. writing—original draft; M. S. writing—review and editing.

Conflict of interest—The authors declare no conflict of interest with regard to this work.

Abbreviations—The abbreviations used are: 4'-PP, 4'-phosphopantetheine; ACP, acyl carrier protein; CoA, coenzyme A; DSS, sodium 4,4-dimethyl-4-silapentanesulfonate; ESI-MS, electrospray ionization–mass spectrometry; FAS, fatty acid synthesis; HSQC, heteronuclear single quantum coherence spectroscopy; NMR, nuclear magnetic resonance; ScACP, *Saccharomyces cerevisiae* acyl carrier protein; SEC, size-exclusion chromatography.

References

- Maier, T., Leibundgut, M., and Ban, N. (2008) The crystal structure of a mammalian fatty acid synthase. *Science* **321**, 1315
- Leibundgut, M., Jenni, S., Frick, C., and Ban, N. (2007) Structural basis for substrate delivery by acyl carrier protein in the yeast fatty acid synthase. *Science* **316**, 288
- Zhu, Z., Zhou, Y. J., Krivoruchko, A., Grininger, M., Zhao, Z. K., and Nielsen, J. (2017) Expanding the product portfolio of fungal type I fatty acid synthases. *Nat. Chem. Biol.* **13**, 360–362
- Roujeinikova, A., Simon, W. J., Gilroy, J., Rice, D. W., Rafferty, J. B., and Slabas, A. R. (2007) Structural studies of fatty acyl-(acyl carrier protein) thioesters reveal a hydrophobic binding cavity that can expand to fit longer substrates. *J. Mol. Biol.* **365**, 135–145
- Zornetzer, G. A., Fox, B. G., and Markley, J. L. (2006) Solution structures of spinach acyl carrier protein with decanoate and stearate. *Biochemistry* **45**, 5217–5227
- Sharma, A. K., Sharma, S. K., Surolia, A., Surolia, N., and Sarma, S. P. (2006) Solution structures of conformationally equilibrium forms of holo-acyl carrier protein (PfACP) from *Plasmodium falciparum* provides insight into the mechanism of activation of ACPs. *Biochemistry* **45**, 6904–6916
- Upadhyay, S. K., Misra, A., Srivastava, R., Surolia, N., Surolia, A., and Sundd, M. (2009) Structural insights into the acyl intermediates of the *Plasmodium falciparum* fatty acid synthesis pathway: The mechanism of expansion of the acyl carrier protein core. *J. Biol. Chem.* **284**, 22390–22400
- Arya, R., Sharma, B., Dhembla, C., Pal, R. K., Patel, A. K., Sundd, M., Ghosh, B., Makde, R. D., and Kundu, S. (2019) A conformational switch from a closed apo- to an open holo-form equips the acyl carrier protein for acyl chain accommodation. *Biochim. Biophys. Acta Proteins Proteom.* **1867**, 163–174
- Revell, W. P., Bibb, M. J., and Hopwood, D. A. (1996) Relationships between fatty acid and polyketide synthases from *Streptomyces coelicolor* A3(2): Characterization of the fatty acid synthase acyl carrier protein. *J. Bacteriol.* **178**, 5660–5667
- Roujeinikova, A., Baldock, C., Simon, W. J., Gilroy, J., Baker, P. J., Stuitje, A. R., Rice, D. W., Slabas, A. R., and Rafferty, J. B. (2002) X-ray crystallographic studies on butyryl-ACP reveal flexibility of the structure around a putative acyl chain binding site. *Structure* **10**, 825–835
- Cronan, John E. (2014) The chain-flipping mechanism of ACP (acyl carrier protein)-dependent enzymes appears universal. *Biochem. J.* **460**, 157–163
- Nguyen, C., Haushalter, R. W., Lee, D. J., Markwick, P. R. L., Bruegger, J., Caldara-Festin, G., Finzel, K., Jackson, D. R., Ishikawa, F., O'Dowd, B., McCammon, J. A., Opella, S. J., Tsai, S.-C., and Burkart, M. D. (2014)

A GX₂GX₃G motif facilitates chain sequestration in yeast ACP

- Trapping the dynamic acyl carrier protein in fatty acid biosynthesis. *Nature* **505**, 427–431
- Sztain, T., Bartholow, T. G., Lee, D. J., Casalino, L., Mitchell, A., Young, M. A., Wang, J., McCammon, J. A., and Burkart, M. D. (2021) Decoding allosteric regulation by the acyl carrier protein. *Proc. Natl. Acad. Sci. U. S. A.* **118**, e2025597118
 - Ploskoń, E., Arthur, C. J., Evans, S. E., Williams, C., Crosby, J., Simpson, T. J., and Crump, M. P. (2008) A mammalian type I fatty acid synthase acyl carrier protein domain does not sequester acyl chains. *J. Biol. Chem.* **283**, 518–528
 - Lou, J. W., Iyer, K. R., Hasan, S. M. N., Cowen, L. E., and Mazhab-Jafari, M. T. (2019) Electron cryomicroscopy observation of acyl carrier protein translocation in type I fungal fatty acid synthase. *Sci. Rep.* **9**, 12987
 - Perez, D. R., Leibundgut, M., and Wider, G. (2015) Interactions of the acyl chain with the *Saccharomyces cerevisiae* acyl carrier protein. *Biochemistry* **54**, 2205–2213
 - Nguyen, L. N., Cesar, G. V., Le, G. T. T., Silver, D. L., Nimricher, L., and Nosnachuk, J. D. (2012) Inhibition of *Candida parapsilosis* fatty acid synthase (Fas2) induces mitochondrial cell death in serum. *PLoS Pathog.* **8**, e1002879
 - Zhao, X. J., McElhaney-Feser, G. E., Bowen, W. H., Cole, M. F., Broedel, S. E., Jr., and Cihlar, R. L. (1996) Requirement for the *Candida albicans* FAS2 gene for infection in a rat model or oropharyngeal candidiasis. *Microbiology* **142**, 2509–2514
 - Perez, D. R., and Wider, G. (2009) 1H, 15N, 13C resonance assignment of the acyl carrier protein subunit of the *Saccharomyces cerevisiae* fatty acid synthase. *Biomol. NMR Assign.* **3**, 133–136
 - Willard, L., Ranjan, A., Zhang, H., Monzavi, H., Boyko, R. F., Sykes, B. D., and Wishart, D. S. (2003) VADAR: A web server for quantitative evaluation of protein structure quality. *Nucleic Acids Res.* **31**, 3316–3319
 - Pettersen, E. F., Goddard, T. D., Huang, C. C., Couch, G. S., Greenblatt, D. M., Meng, E. C., and Ferrin, T. E. (2004) UCSF Chimera—a visualization system for exploratory research and analysis. *J. Comput. Chem.* **25**, 1605–1612
 - Williamson, M. P. (2013) Using chemical shift perturbation to characterise ligand binding. *Prog. Nucl. Magn. Reson. Spectrosc.* **73**, 1–16
 - Akasaka, K., Li, H., Yamada, H., Li, R., Thoresen, T., and Woodward, C. K. (1999) Pressure response of protein backbone structure. Pressure-induced amide 15N chemical shifts in BPTI. *Protein Sci.* **8**, 1946–1953
 - Hori, S., Yamauchi, K., Kuroki, S., and Ando, I. (2002) Proton NMR chemical shift behavior of hydrogen-bonded amide proton of glycine-containing peptides and polypeptides as studied by *ab initio* MO calculation. *Int. J. Mol. Sci.* **3**, 907–913
 - de Dios, A. C., and Oldfield, E. (1994) Chemical shifts of carbonyl carbons in peptides and proteins. *J. Am. Chem. Soc.* **116**, 11485–11488
 - Asakawa, N., Kuroki, S., Kurosu, H., Ando, I., Shoji, A., and Ozaki, T. (1992) Hydrogen-bonding effect on carbon-13 NMR chemical shifts of L-alanine residue carbonyl carbons of peptides in the solid state. *J. Am. Chem. Soc.* **114**, 3261–3265
 - Shen, Y., Delaglio, F., Cornilescu, G., and Bax, A. (2009) TALOS plus: A hybrid method for predicting protein backbone torsion angles from NMR chemical shifts. *J. Biomol. NMR* **44**, 213–223
 - Kumar, P., and Bansal, M. (2012) HELANAL-plus: A web server for analysis of helix geometry in protein structures. *J. Biomol. Struct. Dyn.* **30**, 773–783
 - Tian, W., Chen, C., Lei, X., Zhao, J., and Liang, J. (2018) CASTp 3.0: Computed atlas of surface topography of proteins. *Nucleic Acids Res.* **46**, 363–367
 - Voss, N. R., and Gerstein, M. (2010) 3V: Cavity, channel and cleft volume calculator and extractor. *Nucleic Acids Res.* **38**, W555–W562
 - Hall, S. E., Roberts, K., and Vaidehi, N. (2009) Position of helical kinks in membrane protein crystal structures and the accuracy of computational prediction. *J. Mol. Graph. Model.* **27**, 944–950
 - Högel, P., Götz, A., Kuhne, F., Ebert, M., Stelzer, W., Rand, K. D., Scharnagl, C., and Langosch, D. (2018) Glycine perturbs local and global conformational flexibility of a transmembrane helix. *Biochemistry* **57**, 1326–1337
 - Horn, R., Ahern, C. A., and Ding, S. (2005) Investigating the putative glycine hinge in shaker potassium channel. *J. Gen. Physiol.* **126**, 213–226
 - Grottesi, A., Domene, C., Hall, B., and Sansom, M. S. P. (2005) Conformational dynamics of M2 helices in KirBac channels: helix flexibility in relation to gating *via* molecular dynamics simulations. *Biochemistry* **44**, 14586–14594
 - Zhao, Y., Yarov-Yarovoy, V., Scheuer, T., and Catterall, W. A. (2004) A gating hinge in Na⁺ channels; a molecular switch for electrical signaling. *Neuron* **41**, 859–865
 - Pedetta, A., Massazza, D. A., Seitz, M. K. H., and Studdert, C. A. (2017) Mutational replacements at the “glycine hinge” of the *Escherichia coli* chemoreceptor Tsr support a signaling role for the C-helix residue. *Biochemistry* **56**, 3850–3862
 - Wilman, H. R., Shi, J., and Deane, C. M. (2014) Helix kinks are equally prevalent in soluble and membrane proteins. *Proteins* **82**, 1960–1970
 - Gorner, K., Holtorf, E., Waak, J., Phan, T. T., Weisenhorn-Vogt, D. M., Wurst, W., Haass, C., and Kahle, P. J. (2007) Structural determinants of the C-terminal helix-kink-helix motif essential for protein stability and survival promoting activity of DJ-1. *J. Biol. Chem.* **282**, 13680–13691
 - McAndrew, R. P., Wang, Y., Mohsen, A.-W., He, M., Vockley, J., and Kim, J.-J. P. (2008) Structural basis for substrate fatty acyl chain specificity: crystal structure of human very-long-chain acyl-CoA dehydrogenase. *J. Biol. Chem.* **283**, 9435–9443
 - van Aalten, D. M. F., Jones, P. C., Sousa, M. de., and Findlay, J. B. C. (1997) Engineering protein mechanics: Inhibition of concerted motions of the cellular retinol binding protein by site-directed mutagenesis. *Protein Eng.* **10**, 31–37
 - van Aalten, D. M. F., Amadei, A., Linssen, A. B. M., Eijssink, V. G. H., Vriend, G., and Berendsen, H. J. C. (1995) The essential dynamics of thermolysin-conformation of the hinge-bending motion and comparison of simulations in vacuum and water. *Proteins* **22**, 45–54
 - Dongre, M., Singh, N. S., Dureja, C., Peddada, N., Solanki, A. K., and Raychaudhuri, S. (2011) Evidence on how a conserved glycine in the hinge region of HapR regulates its DNA binding ability: Lessons from a natural variant. *J. Biol. Chem.* **286**, 15043–15049
 - Di Scala, C., Chahinian, H., Yahi, N., Garmy, N., and Fantini, J. (2014) Interaction of Alzheimer’s β -amyloid peptides with cholesterol: Mechanistic insights into amyloid pore formation. *Biochemistry* **53**, 4489–4502
 - Barrett, P. J., Song, Y., Van Horn, W. D., Hustedt, E. J., Schafer, J. M., Hadziselimovic, A., Beel, A. J., and Sanders, C. R. (2012) The amyloid precursor protein has a flexible transmembrane domain and binds cholesterol. *Science* **336**, 1168
 - Ballesteros, J. A., Deupi, X., Olivella, M., Haaksma, E. E., and Pardo, L. (2000) Serine and threonine residues bend alpha-helices in the chi(1) = g(-) conformation. *Biophys. J.* **79**, 2754–2760
 - Gray, T., and Matthews, B. (1984) Intrahelical hydrogen bonding of serine, threonine and cysteine residues within α -helices and its relevance to membrane-bound proteins. *J. Mol. Biol.* **175**, 75–81
 - Ambrosio, C., Molinari, P., Cotecchia, S., and Costa, T. (2000) Catechol-binding serines of β 2-adrenergic receptors control the equilibrium between active and inactive receptor states. *Mol. Pharmacol.* **57**, 198–210
 - Hu, W., Zhang, Y., Sun, X., Zhang, T., Xu, L., Xie, H., Li, Z., Liu, W., Lou, J., and Chen, W. (2019) FcyRIIB-I232T polymorphic change allosterically suppresses ligand binding. *Elife* **8**, e46689
 - Delaglio, F., Grzesiek, S., Vuister, G. W., Zhu, G., Pfeifer, J., and Bax, A. (1995) NMRPipe: A multidimensional spectral processing system based on UNIX pipes. *J. Biomol. NMR* **6**, 277–293
 - Goddard, T., and Kneller, D. (2008) *Sparky 3*, University of California, San Francisco, USA
 - Wishart, D. S., Bigam, C. G., Yao, J., Abildgaard, F., Dyson, H. J., Oldfield, E., Markley, J. L., and Sykes, B. D. (1995) 1H, 13C and 15N chemical shift referencing in biomolecular NMR. *J. Biomol. NMR* **6**, 135–140
 - Grzesiek, S., Bax, A., Clore, G. M., Gronenborn, A. M., Hu, J. S., Kaufman, J., Plamer, I., Stahl, S. J., and Wingfield, P. T. (1996) The solution structure of HIV-1 Nef reveals an unexpected fold and permits delineation of the binding surface for the SH3 domain of Hck tyrosine protein kinase. *Nat. Struct. Biol.* **3**, 340–345